

Design and Analysis of a Miniaturized Atomic Force Microscope Scan Head



B. N. Arya  and G. R. Jayanth 

Abstract The Atomic Force Microscope (AFM) finds widespread applications as a tool for nano-scale characterization studies and atomic manipulation. Here, we propose the design of a miniaturized AFM scan head for 3-axis nano-positioning. The scan head uses parallelogram-based flexures for amplifying displacements in-plane and a bridge-type displacement amplifier for out-of-plane positioning and achieves a displacement range of $\pm 5 \mu\text{m}$ along X -, Y - and Z -axes. Subsequently, a lumped parameter model has been obtained for analysing the quasi-static and dynamic characteristics of the different subsystems of the positioner. A comparison of the analytical expressions for the displacement gain and eigen frequencies with Finite Element (FE) analysis revealed match to within 4%. The bandwidth along Z -axis is about 5 kHz, which is much larger than that of a conventional AFM scan head. Finally, a feedback control system has been designed to achieve position control using model inversion.

Keywords Compact AFM · Displacement amplifier · Model inversion

1 Introduction

An Atomic Force Microscope (AFM) is a type of scanning probe microscope used for nano-scale characterization, topography imaging and manipulation of conducting and insulating samples, at sub-nanometer resolution. Conventional AFM systems possess certain limitations which affect the quality of their measurement results such as low speed, small scan area and the effect of actuation nonlinearities. Another important limitation arises from its bulky nature. By exploiting the benefits of scaling laws, it has long been known that a compact construction can make the AFM system immune to these limitations [1].

B. N. Arya (✉) · G. R. Jayanth
Indian Institute of Science, Bangalore 560012, India
e-mail: aryanair@iisc.ac.in

G. R. Jayanth
e-mail: jayanth@iisc.ac.in

The first compact AFM designs featured a single-chip CMOS-based AFM with integrated sensing and actuating mechanisms such as piezoresistive sensing, thermal bimorph actuators [2] and electrothermal actuators [3], while others used a combination of electrostatic and electrothermal actuators, along with an integrated piezoelectric layer for fine positioning along X -, Y - and Z -axes, respectively [4]. Such integrated single-chip systems require complex signal routing circuitry. The use of electrothermal actuators also poses certain limitations such as reduced scan rates due to limited bandwidth, heat dissipation [5] and parasitic resonances. Also, during scanning, AFM tips are found to get damaged frequently, necessitating their replacement. This results in having to discard the entire probe, along with its integrated fine positioning and deflection sensing mechanisms, even when their function remains intact. This contributes to a significantly higher running cost of the instrument. Also, single-chip AFM models impose constraints on the stiffness and geometry of the probe that they can support, which greatly reduces their flexibility.

Therefore, here we propose a compact design for the fine positioning mechanism, on which a conventional AFM probe can be placed, as opposed to integrating them on a consumable such as a cantilever. This enables retaining the high bandwidth and compactness without having to discard these systems when the tip gets blunted. The designs of the fine positioner are based on flexure-based displacement amplifiers actuated by miniature piezo actuators. The use of displacement amplifiers enables a compact construction with large motion ranges along X -, Y - and Z -axes, compared to in-plane positioners that employ compliant beams for just guiding motion and not for amplifying it [6]. Such a compact design also allows the easy integration of any deflection measurement technique such as piezoresistive sensors. The quasi-static and dynamic models of these structures have been developed. Finally, a feedback control system using model inversion technique has been designed for regulating the motion of the positioners by actuating the piezo actuators accordingly.

The rest of the paper is divided as follows. Section 2 discusses the design of the positioning mechanisms. Sections 3 and 4 describe quasi-static modelling using Pseudo Rigid Body Models (PRBM) and eigen-frequency analysis using Rayleigh's technique, respectively. Section 5 discusses feedback control using model inversion. Finally, conclusions are presented in Sect. 6.

2 Design of Fine Positioner of the Miniaturized AFM

Figure 1a shows the geometric model of the fine positioner for a miniaturized AFM system. It consists of flexure-based amplifiers which employs parallel kinematics for achieving nano-scale displacements along X -, Y - and Z -axes. In particular, it consists of three main components, namely the in-plane positioner, which is designed for motion along X - and Y -axes, the out-of-plane positioner which is designed for motion along Z -axis and a decoupling stage in between the two, for decoupling the motion between the in-plane and out-of-plane positioner.

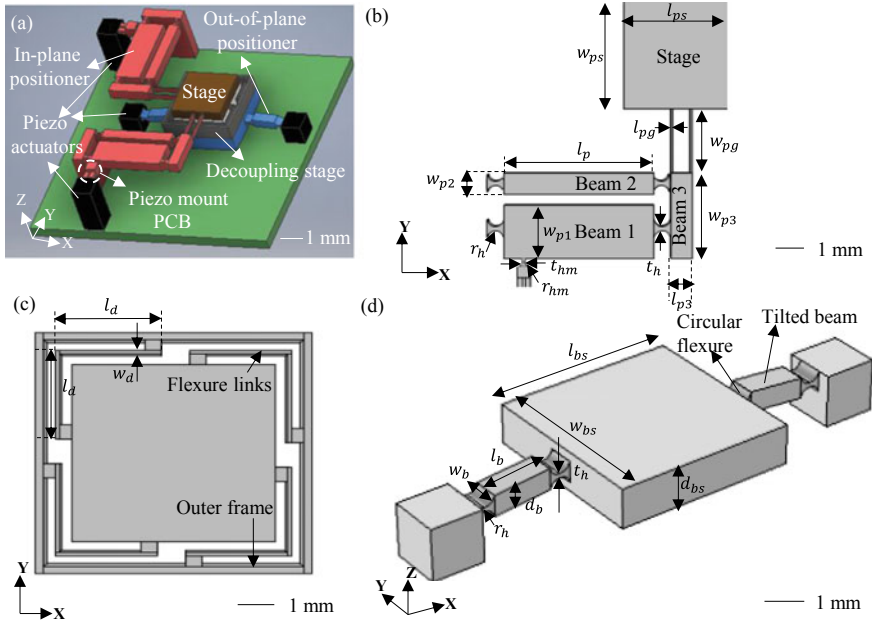


Fig. 1 Computer-Aided Design (CAD) model of **a** fine positioner, **b** in-plane positioner, **c** decoupling stage, **d** out-of-plane positioner

The in-plane positioner consists of parallelogram flexures (Beam 1 and Beam 2 in Fig. 1b) with circular flexure hinges at either ends of the beam, connected to an output beam (Beam 3 in Fig. 1b). They constitute a lever-based amplifier design and achieve amplified motion along X- and Y-axes. The motion between the two axes is decoupled by using thin flexure guided beams, which connect the output beam of the amplifier to a stage block. Shear chip piezo actuators are chosen for actuating the in-plane positioners. To decouple the angular motion of the parallelogram flexure from the motion of the shear piezo actuator, a circular flexure hinge-based piezo mount with a pair of guided beams is used to connect the two. The guided beams are employed to decouple transverse motion of the parallelogram flexure at its point of connection to the circular hinge from the motion of the piezo actuator (Fig. 1b).

The decoupling stage serves the purpose of decoupling the in-plane motion of the in-plane positioner, from that of the out-of-plane positioner while coupling the out-of-plane motion of the positioner to that of the stage. The decoupling stage is composed of a central platform around which 4 L-shaped flexure links are positioned symmetrically (Fig. 1c). This structure is then connected to an outer frame. The central platform connects to the stage of the in-plane positioner while the outer frame connects to the out-of-plane positioner. The interconnecting flexures are designed to achieve high compliance along X- and Y- axes and high stiffness along the Z-axis.

The out-of-plane positioning mechanism consists of a bridge-type displacement amplifier. The mechanism comprises 3 nearly rigid tilted beams connected by circular

Table 1 Dimensions for the different elements of the fine positioner

	Parameter	Dimension (mm)	Parameter	Dimension (mm)
In-plane positioner	l_p	3.5	t_h	0.1
	w_{p1}	1.25	r_h	0.2
	w_{p2}	0.5	l_{pg}	0.05
	l_{p3}	0.5	w_{pg}	1.5
	w_{p3}	2	$l_{ps} = w_{ps}$	2.5
	t_{hm}	0.05	r_{hm}	0.05
Decoupling stage	l_d	1.3	w_d	0.05
Out-of-plane positioner	l_b	1.1	$l_{bs}=w_{bs}$	3.4
	$w_b=d_b$	0.4	d_{bs}	0.75

flexure hinges (Fig. 1d). The two tilted beams are identical in length and are tilted by the same angle to the horizontal. When an input displacement is provided along X -direction by means of shear chip piezo actuators, an amplified output is obtained along Z -axis. Here, the displacement gain is only dependent on the angle of inclination of the beam and hence provides greater flexibility in design for higher amplification ratios, without taking up additional space.

The dimensions of the different elements in the positioners are shown in Table 1. The depth of all the elements was taken as 0.5 mm, unless specified otherwise.

3 Quasi-Static Modelling and Analysis of the Fine Positioners

Quasi-static modelling involves developing lumped parameter models for the constituent compliant elements of the positioner. In all cases where bending deformations are involved, Euler–Bernoulli beam theory [7] has been employed to analyse the deformations.

3.1 In-Plane Positioner

The model of the parallelogram flexure consists of two beams (Beam 1 and Beam 2) that form the sides of the parallelogram, connected by circular flexure hinges to an output beam (Beam 3) (Fig. 1b). Beams 1 and 2 are both modelled as elastic beams, and Beam 3 is assumed to be nearly rigid. The length of the beams is denoted by l_p , and their width is denoted by w_{p1} and w_{p2} for Beam 1 and Beam 2, respectively. The circular flexures are modelled as torsional hinges with torsional stiffness k_{θ_p} .

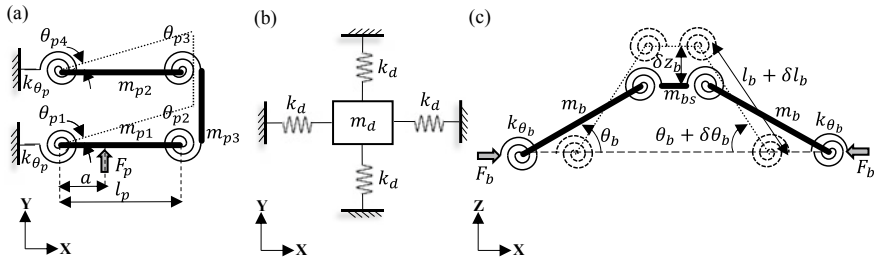


Fig. 2 Lumped parameter model of **a** in-plane positioner, **b** decoupling stage, **c** out-of-plane positioner

The angular displacement of the i^{th} hinges ($i = 1 \dots 4$) is given by the variables θ_{pi} (Fig. 2a).

The expression for output displacement of the parallelogram flexure was derived by considering a force F_p applied at a distance a from the point of rotation of the fixed hinges to Beam 1. If f_p is the reaction force that Beam 3 applies on Beam 1, and $y_{p1}(x)$ and $y_{p2}(x)$ represent the deformation profiles of the Beams 1 and 2, then the boundary conditions are given by $y_{p1}(l_p) = y_{p2}(l_p)$, $\left(\frac{dy_{p1}}{dx}\right)_{x=0} = \theta_{p1}$, $\left(\frac{dy_{p1}}{dx}\right)_{x=l_p} = \theta_{p2}$, $\left(\frac{dy_{p2}}{dx}\right)_{x=l_p} = \theta_{p3}$, $\left(\frac{dy_{p2}}{dx}\right)_{x=0} = \theta_{p4}$. Also, by moment balance it can be seen that $(F_p - f_p) = \frac{k_{\theta_p}}{a}(\theta_{p1} + \theta_{p2})$ and $f_p = \frac{k_{\theta_p}}{a}(\theta_{p3} + \theta_{p4})$. The value of k_{θ_p} was estimated from the Paros–Weisbord equations [8] and is dependent on r_h , the radius of curvature, and t_h , the thickness of the hinge (Fig. 1b).

By applying these boundary conditions and using Euler–Bernoulli beam theory, $y_{p1}(x)$ and $y_{p2}(x)$ were obtained to be

$$y_{p1}(x) = \begin{cases} \left(\frac{f_p - F_p}{6EI_{p1}}\right)x^3 + \left(\frac{F_p a - f_p l_p - k_{\theta_p} \theta_{p2}}{2EI_{p1}}\right)x^2 + \theta_{p1}x & \text{for } x \leq a \\ \left(\frac{f_p}{6EI_{p1}}\right)x^3 - \left(\frac{f_p l_p + k_{\theta_p} \theta_{p2}}{2EI_{p1}}\right)x^2 + \left(\frac{F_p a^2}{2EI_{p1}} + \theta_{p1}\right)x - \frac{F_p a^3}{6EI_{p1}} & \text{for } x \geq a \end{cases} \quad (1)$$

$$y_{p2}(x) = \left(\frac{-f_p}{6EI_{p2}}\right)x^3 - \left(\frac{f_p l_p - k_{\theta_p} \theta_{p3}}{2EI_{p2}}\right)x^2 + \theta_{p4}x \quad (2)$$

where x is the distance from the fixed end of the beam, I_{p1} and I_{p2} are the area moments of inertia of Beams 1 and 2, respectively, and E is the Young's modulus. By applying the boundary conditions, all the variables can be obtained in terms of the input force F_p . Normalizing the reaction force, f_p , and input force, F_p as $\tilde{f}_p = \frac{f_p}{k_{\theta_p} a}$ and $\tilde{F}_p = \frac{F_p}{k_{\theta_p} a}$, the angles and the normalized reaction force can be obtained by solving the following equation:

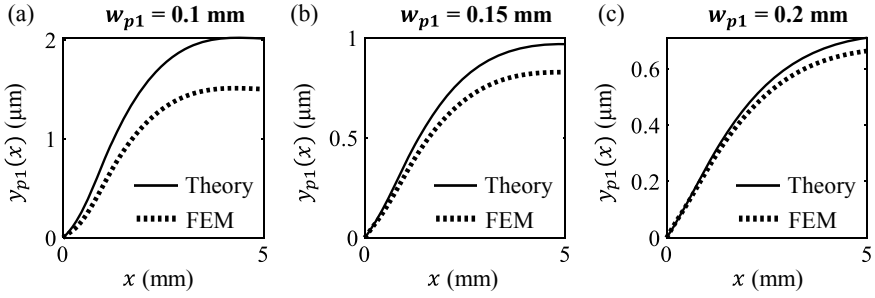


Fig. 3 Comparison of analytical and FEM simulation results for displacement profile of Beam 1, for $F_p = 1$ mN and $l_p = 5$ mm and **a** $w_{p1} = 0.1$ mm, **b** $w_{p1} = 0.15$ mm, **c** $w_{p1} = 0.2$ mm

$$\begin{bmatrix}
 0 & 1 & 1 & 1 & 1 \\
 1 & 0 & 0 & -1 & -1 \\
 \frac{k_{\theta_p} l_p}{2E I_{p2}} & 0 & 0 & -\left(1 + \frac{k_{\theta_p} l_p}{E I_{p2}}\right) & 1 \\
 \frac{k_{\theta_p} l_p}{2E I_{p1}} & -1 & \left(1 + \frac{k_{\theta_p} l_p}{E I_{p1}}\right) & 0 & 0 \\
 \left(\frac{k_{\theta_p} l_p^2}{3E I_{p1}} + \frac{k_{\theta_p} l_p^2}{3E I_{p2}}\right) & -l_p & \frac{k_{\theta_p} l_p^2}{2E I_{p1}} & -\frac{k_{\theta_p} l_p^2}{2E I_{p2}} & l_p
 \end{bmatrix}
 \begin{bmatrix}
 \tilde{f}_p \\
 \theta_{p1} \\
 \theta_{p2} \\
 \theta_{p3} \\
 \theta_{p4}
 \end{bmatrix}
 =
 \begin{bmatrix}
 1 \\
 0 \\
 0 \\
 \frac{k_{\theta_p} a}{2E I_{p1}} \\
 \frac{k_{\theta_p} a(3l_p - a)}{6E I_{p1}}
 \end{bmatrix}
 \tilde{F}_p
 \quad (3)$$

To validate these results, the deformation profile $y_{p1}(x)$ of Beam 1 has been plotted for three different values of beam width, namely $w_{p1} = 0.1, 0.15, 0.2$ mm (Fig. 3) and the results have been compared with those of Finite Element (FE) analysis.

The percentage error between analytical and FE results is only 6% for $w_{p1} = 0.2$ mm and is less than 30% for slender beams, for an input force of $F_p = 1$ mN. The greater mismatch between the two plots for slender beams suggests incorrect assumption in modelling the flexure hinges as torsional springs for the case of slender beams. However, since wider and stiffer parallelogram beams are preferred for amplified in-plane displacement, the effect of the mismatch is not significant from the point of view of design.

3.2 Decoupling Stage

The decoupling stage consists of 4 L-shaped flexure links connected to a central platform. Each of these flexures is modelled as linear springs of stiffness k_d (Fig. 2b), placed symmetrically around a rigid central platform. During in-plane motion, the longitudinal element of the flexures undergoes axial deformation, and the lateral element undergoes transverse deformation. Thus, the single flexure link can be modelled as a series combination of two linear springs with effective stiffness $k_{d\text{eff}}$ given by

Table 2 Comparison of analytical and FEM results for effective stiffness of decoupling stage and out-of-plane fine positioner

Parameter	Theory	FEM	Error (%)
$k_{d\text{eff}}$ (kN/m)	8.95	9.79	8.58
$k_{b\text{eff}}$ (kN/m)	43.03	42.49	-1.27

$$k_d = \frac{k_{d\text{ax}}k_{d\text{tr}}}{k_{d\text{ax}} + k_{d\text{tr}}} \quad (4)$$

where $k_{d\text{tr}} = \frac{12EI_d}{l_d^3}$ is the transverse stiffness and $k_{d\text{ax}} = \frac{EA_d}{l_d}$ is the axial stiffness of the flexure link. Here, I_d , A_d and l_d are the area moment of inertia, area of cross section and length of the flexure link, respectively. Since all the 4-flexure links have similar dimensions and undergo same amount of deformation, the total effective stiffness is given by $k_{d\text{eff}} = 4k_d$. Due to the symmetric nature of the geometry, estimating the displacement profile along either X - or Y -axis is sufficient. Thus, considering an input force F_d applied along X -axis, the output displacement δx_d , is given by

$$\delta x_d = \frac{F_d}{k_{d\text{eff}}} = \frac{F_d}{4k_d} \quad (5)$$

For an input force of $F_d = 0.1$ N, the comparison between Finite Element Method (FEM) and analytical results for the effective in-plane stiffness shows a match of 8.6% (Table 2).

3.3 Out-of-Plane Positioner

The bridge displacement amplifier consists of two tilted beams, attached to a cuboidal platform through circular flexure hinges. The tilted beams are modelled as elastic beams of length l_b , and the circular flexures are modelled as torsional hinges of stiffness k_{θ_b} . When an external input force F_b is applied along X -axis at the ends of the tilted beams, they undergo compression by an amount δl_b and the circular hinges undergo rotation by an amount $\delta \theta_b$, resulting in an output displacement, δz_b , of the cuboidal platform along Z -axis (Fig. 2c).

The effective stiffness of the bridge amplifier along Z -axis is then estimated by equating the total potential energy of the amplifier to the potential energy stored in an equivalent lumped model with an effective stiffness $k_{b\text{eff}}$ as,

$$4\left(\frac{1}{2}k_{\theta_b}\delta\theta_b^2\right) + 2\left(\frac{1}{2}k_{b_x}\delta l_b^2\right) = \frac{1}{2}k_{b\text{eff}}\delta z_b^2 \quad (6)$$

where k_{b_x} is the effective longitudinal stiffness of the elastic beam, comprising of the series combination of the longitudinal stiffness of the 2 circular hinges [7] and the

tilted flexure beams. Simplifying Eq. (6) and using moment balance equations for a force component acting along the length of the tilted beam, the output displacement, δz_b , can be written as:

$$z_b = F_b \sin 2\theta_b \left(\frac{k_{b_x} l_b^2 - 2k_{\theta_b}}{4k_{\theta_b} k_{b_x}} \right) \tag{7}$$

For an input force of $F_b = 1 \mu\text{N}$, the comparison between FEM and analytical results for the effective Z-axis stiffness shows a match of 1.3% (Table 2).

By incorporating the above design considerations, the individual elements of the fine positioner, namely the in-plane positioner, decoupling stage and the out-of-plane positioner, were assembled along with the piezo actuators and their motion along X-, Y- and Z-axes was studied. The stiffness along the in-plane and out-of-plane directions for each of them was also estimated in FEM by applying a point load of $1 \mu\text{N}$. The in-plane positioner offers much lower stiffness along Z-axis (2.21 kN/m) than along X- and Y-axes (46.02 kN/m). The X–Y stiffness is itself much smaller than that of the driving piezo actuators, thereby ensuring that the displacement of the actuators is transmitted almost completely to the stage.

The stiffness of the decoupling stage along X- and Y-axes (9.78 kN/m) is almost 5 times less than that of the in-plane positioner. The decoupling stage has a Z-axis stiffness (94.72 kN/m) which is almost 43 times higher than that of the in-plane positioner, in accordance with the requirement to couple the out-of-plane motion of the Z-positioner placed below it to the sample stage. The Z-axis stiffness of the out-of-plane positioner is 37.70 kN/m, which is much higher than the out-of-plane stiffness of the in-plane positioner but lower than that of the decoupling stage. Therefore, the Z-positioner would couple its displacement to the sample stage, with an attenuation of about 28%.

To verify parasitic motion, the percentage of cross-axis displacements of the fine positioner has been estimated along all the 3 axes and shown in Fig. 4. For X-axis positioning (Fig. 4a), for a maximum output displacement of $23 \mu\text{m}$, the percentage

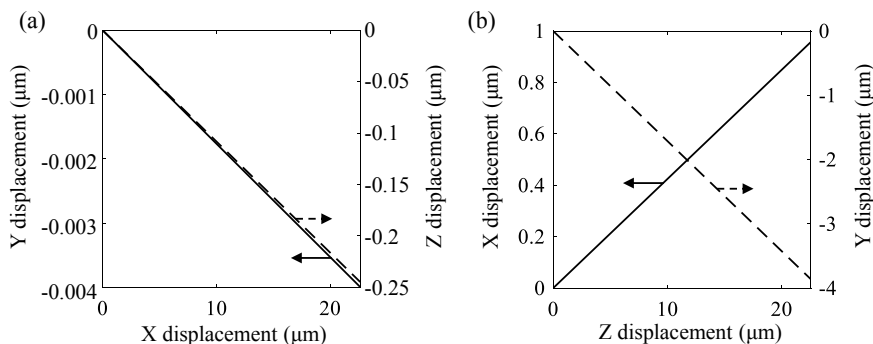


Fig. 4 Plot of **a** Y and Z cross-axis displacement for X-axis positioning and **b** X- and Y-cross-axis displacement for Z-axis positioning, for an input displacement of $5 \mu\text{m}$

of Y - and Z -axis cross-axis displacement is 0.02 and 1.08%, respectively. Similar results have also been obtained for Y -axis positioning owing to the symmetry of the in-plane positioner. Similarly, for Z -axis motion, the percentage of X - and Y -axis cross-coupling is 4 and 17%, respectively (Fig. 4b).

4 Eigen-Frequency Analysis of the Fine Positioners

The fundamental eigen frequencies of the different components of the fine positioner were obtained by using the Rayleigh Quotient method [7]. In this method, the first step is to assume an approximate mode shape function, to replicate the first eigen mode, followed by determining the Rayleigh Quotient by equating the maximum kinetic and potential energies of the system. Here, the quasi-static deformation profiles obtained by utilizing the expressions derived in the previous section are employed as the approximate mode shapes; the eigen frequencies of the different positioners are estimated.

4.1 In-Plane Positioner

Due to the high lateral stiffness of the parallelogram flexures (for the dimensions mentioned in Table 1), their contribution to the elastic potential energy is negligible. Hence, only the elastic potential energy of the torsional springs is considered. Therefore, the potential energy, $U_{p_{\max}}$, of the in-plane positioner is given by

$$U_{p_{\max}} = 0.5k_{\theta p} \sum_{i=1}^4 \theta_{pi}^2 \quad (8)$$

The kinetic energy associated with motion of the hinges is negligible in comparison to the beams, and hence, their effects can be ignored. The total kinematic energy would be due to displacements of Beam 1 and Beam 2 which are assumed to be given approximately by Eqs. (1) and (2).

Therefore, the overall maximum kinetic energy $T_{p_{\max}}$ is given by

$$T_{p_{\max}} = \left[\frac{\rho}{2} \left\{ \int_0^{l_p} (A_{p1}y_{p1}^2(x) + A_{p2}y_{p2}^2(x))dx + \int_0^{3r_h+l_p+0.5l_{p3}} A_{p3}y_{p3}^2(x)dx \right\} \right] \omega_p^2 \quad (9)$$

where ω_p is the eigen frequency of the in-plane positioner, ρ is the density of the material used (aluminium), l_{p3} is the width of Beam 3, A_{p1} , A_{p2} and A_{p3} are the

Table 3 Comparison of analytical and FEM results for eigen frequencies of different elements of the fine positioner

	Theory (kHz)	FEM (kHz)	Error (%)
In-plane positioner	2.63	2.62	-0.38
Decoupling stage	5.18	5.28	1.89
Out-of-plane positioner	6.40	6.71	4.62

area of cross sections, and y_{p1} , y_{p2} and y_{p3} are the maximum modal displacement vectors of Beams 1, 2 and 3, respectively. By writing $T_{p_{\max}} = (t_{p_{\max}} \omega_p^2)$, we can obtain the approximate eigen frequency from Eqs. (8) and (9) as $\omega_p^2 = \frac{U_{p_{\max}}}{t_{p_{\max}}}$.

The comparison of results for FEM and analytical expression shows an error of approximately 0.4% (Table 3).

4.2 Decoupling Stage

The dynamic model of the decoupling stage is obtained by assuming the potential energy of the flexure links alone, owing to their slender geometry as compared to the central platform (Table 1). However, for estimating the kinetic energy, the central stage alone is assumed to contribute, since its mass is significantly higher than that of the flexures. Similar to the method described in Sect. 4.1, Rayleigh technique is used to compute the maximum potential energy of the decoupling stage, $U_{d_{\max}}$, as

$$U_{d_{\max}} = 0.5k_{d_{\text{eff}}}\delta x_d^2 \quad (10)$$

and kinetic energy, $T_{d_{\max}}$,

$$T_{d_{\max}} = 0.5m_d\delta x_d^2\omega_d^2 \quad (11)$$

where m_d and ω_d are the mass and eigen frequency of the decoupling stage, respectively. Here, δx_d and $k_{d_{\text{eff}}}$ are taken from Eq. (5). The comparison of results for FEM and analytical expression shows an error of approximately 2% (Table 3).

4.3 Out-of-Plane Positioner

Here, the potential energy of the model is the combination of the potential energy stored in the 4 circular flexure hinges and the 2 rigid beams. The total kinetic energy is considered to be primarily due to the motion of the central block and the two

beams. Thus, the maximum potential energy $U_{b\max}$ is

$$U_{b\max} = 4\left(\frac{1}{2}k_{\theta_b}\delta\theta_b^2\right) + 2\left(\frac{1}{2}k_{b_x}\delta l_b^2\right) \quad (12)$$

and the maximum kinetic energy $T_{b\max}$ is

$$T_{b\max} = 0.5(2m_b + m_{bs})\delta z_b^2\omega_b^2, \quad (13)$$

where m_b and m_{bs} are the masses of the tilted beams and the central stage platform, respectively, and ω_b is the eigen frequency of the bridge amplifier. Here, δz_b and k_{b_x} are taken from Eq. (7). The comparison of results for FEM and analytical expression shows an error of approximately 5% (Table 3).

5 Feedback Control

The 3-axis positioning mechanism needs to be operated in a feedback control loop to compensate for the nonlinearities introduced by the piezoelectric actuators, such as hysteresis and creep. For this purpose, firstly the transfer function of the positioner is obtained from the frequency responses, relating their displacements to the applied voltage inputs along the respective directions, namely X -, Y - and Z -axes. Here, the frequency response plots for motion along Z -axis alone are considered, and the exact same steps can be repeated along X - and Y -axes. The Bode displacement plots are obtained in COMSOL, by providing a frequency sweep of amplitude 2500 V and frequency range of 0–50 kHz, with a step size of 0.5 kHz, to the shear piezo actuators of the bridge amplifier. The resultant transfer function, $P(s)$, obtained by using MATLAB function for model identification, namely Identified Frequency Response Data (idfrd), is given by

$$P(s) = \frac{M_1s^5 + M_2s^4 + M_3s^3 + M_4s^2 + M_5s + M_6}{s^6 + N_1s^5 + N_2s^4 + N_3s^3 + N_4s^2 + N_5s + N_6} \quad (14)$$

where $M_1 = -2710$, $M_2 = 1.454 \times 10^9$, $M_3 = -5.097 \times 10^{12}$, $M_4 = 4.315 \times 10^{18}$, $M_5 = -1.24 \times 10^{21}$, $M_6 = 2.718 \times 10^{27}$ and $N_1 = 2619$, $N_2 = 4.267 \times 10^9$, $N_3 = 7.221 \times 10^{12}$, $N_4 = 5.699 \times 10^{18}$, $N_5 = 4.71 \times 10^{21}$ and $N_6 = 2.401 \times 10^{27}$.

The Bode plot of the derived transfer function is superimposed with the frequency response obtained from FEM analysis and is seen to match to a good degree, as shown in Fig. 5a. In view of the poorly damped open-loop dynamics of the positioner, model inversion technique is used to cancel the under-damped poles of the plant transfer function and replace them with critically damped or over damped poles. This method helps in achieving a higher closed loop bandwidth, than what is possible by adopting a conventional controller design.

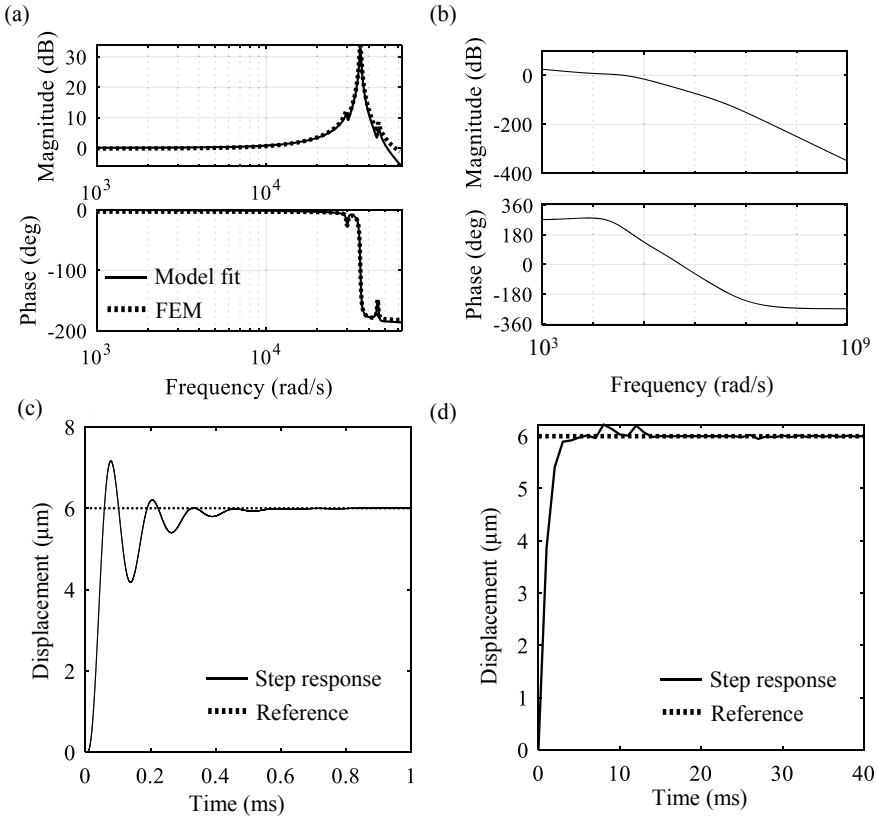


Fig. 5 **a** Model fitting for Z-axis positioning, **b** frequency response plot for Z-axis open-loop gain, **c** step response plot for Z-axis positioning with model inversion, **d** step response plot for Z-axis positioning without model inversion

In this technique, the under-damped minimum-phase poles of the plant, of the form $p_{i\alpha} \pm jp_{i\beta}$ ($i = 1, 2, 3$), are cancelled by the controller zeros and are replaced by critically damped poles with corner frequencies at $\sqrt{p_{i\alpha}^2 + p_{i\beta}^2}$, $i = 1, 2, 3$. Likewise, the minimum-phase zeros are also cancelled. In other words, for the plant transfer function,

$$P(s) = \frac{\prod_{i=1}^m \left(\frac{s}{z_i} + 1 \right)}{\prod_{j=1}^n \left(\frac{s}{p_j} + 1 \right)} \quad (15)$$

the transfer function of the model inversion block, $M(s)$ can be written as

$$M(s) = \frac{\prod_{j=1}^n \left(\frac{s}{p_j} + 1 \right)}{\prod_{i=1}^m \left(\frac{s}{z_i} + 1 \right) \left(\frac{s}{\sqrt{p_{i\alpha}^2 + p_{i\beta}^2}} + 1 \right)} \quad (16)$$

where z_i and p_j denote the zeros and poles of the plant and m and n are the total number of zeros and poles of the plant, respectively. Subsequently, a PID controller is designed to achieve a phase margin of 40° , with proportional (P), integral (I) and derivative (D) gains being $P = 1.89$, $I = 12,600$, $D = 8 \times 10^{-5}$, respectively.

The Bode plot of the overall open-loop system, consisting of the cascade of the plant $P(s)$, the model inversion block $M(s)$ and the compensator or the controller, shows a closed loop bandwidth of 4×10^4 rad/s (Fig. 5b). The closed loop step response of the model shows a settling time of 0.42 ms and rise time of 32.82 μ s (Fig. 5c). In comparison, the settling time for the system without model inversion is about 100 times larger (Fig. 5d). In addition, the response also shows unmodelled oscillations. Therefore, the performance of the system is drastically improved by incorporating a model inversion function into the feedback loop for closed loop position control.

6 Conclusion

This paper presented the design and analysis of a miniaturized AFM scan head, that can achieve fine positioning in three dimensions. For fine positioning along the in-plane directions, a parallelogram flexure-based displacement amplifier with circular flexure hinges was used. A bridge-type displacement amplifier was designed for out-of-plane fine positioning. A decoupling stage with flexure links was then used to decouple the motion of the in-plane positioner from that of the out-of-plane positioner along the in-plane axes and to couple the motion of the latter to the former along the Z-axis. The volume of the proposed compact design of the fine positioner was $1.2 \times 1.2 \times 0.3$ cm³.

Subsequently, the proposed designs were modelled to study their quasi-static and dynamic behaviour and the theoretically estimated values were found to match with the FEM simulation results with an average error of approximately 4%. Finally, the analytical models of the fine positioners were used to design a feedback control loop using PID control cascaded with model inversion, to enable closed loop position control, with significant improvement over conventional control without model inversion.

References

1. Strathearn D, Sarkar N, Lee G, Olfat M, Mansour RR (2017) The benefits of miniaturization of an atomic force microscope. In: 30th IEEE international conference on micro electro mechanical systems (MEMS), pp 1363–1366. IEEE, Las Vegas, USA
2. Barrettino D, Hafizovic S, Volden T, Sedivy J, Kirstein K, Hierlemann A, Baltes H (2004) CMOS monolithic atomic force microscope. In: Symposium on VLSI circuits. Digest of technical papers (IEEE Cat. No. 04CH37525), pp 306–309. Widerkehr and Associates, Honolulu, HI, USA
3. Sarkar N, Mansour RR, Patange O, Trainor K (2011) CMOS-MEMS atomic force microscope. In: 16th international solid-state sensors, actuators and microsystems conference, pp 2610–2613. IEEE, Beijing, China
4. Ruppert MG, Fowler AG, Maroufi M, Moheimani SOR (2017) On-chip dynamic mode atomic force microscopy: a silicon-on-insulator MEMS approach. *J Microelectromech Syst* 26:215–225. <https://doi.org/10.1109/JMEMS.2016.2628890>
5. Bell DJ, Lu TJ, Fleck NA, Spearing SM (2005) MEMS actuators and sensors: observations on their performance and selection for purpose. *J Micromech Microeng* 15:S153–S164. <https://doi.org/10.1088/0960-1317/15/7/022>
6. Awtar S (2003) Synthesis and analysis of parallel kinematic XY flexure mechanisms
7. Meirovitch L (2010) Fundamentals of vibrations, 1st edn. McGraw-Hill, New York
8. Yong YK, Lu T-F, Handley DC (2008) Review of circular flexure hinge design equations and derivation of empirical formulations. *Precis Eng* 32:63–70. <https://doi.org/10.1016/j.precisioneng.2007.05.002>